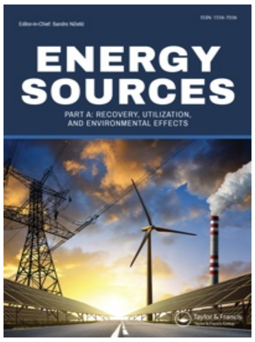

Taylor & Francis
Taylor & Francis Group

Energy Sources, Part A: Recovery, Utilization, and Environmental Effects

ISSN: 1556-7036 (Print) 1556-7230 (Online) Journal homepage: www.tandfonline.com/journals/ueso20

Theoretical and experimental investigations of fixed-focus Fresnel-lens solar collectors with different cavity receivers

Vishwas Mahadeo Palve & Gajanan Namdeorao Shelke

To cite this article: Vishwas Mahadeo Palve & Gajanan Namdeorao Shelke (2026) Theoretical and experimental investigations of fixed-focus Fresnel-lens solar collectors with different cavity receivers, Energy Sources, Part A: Recovery, Utilization, and Environmental Effects, 48:1, 2678537, DOI: 10.1080/15567036.2026.2678537

To link to this article: https://doi.org/10.1080/15567036.2026.2678537

Published online: 27 May 2026.

ENERGY SOURCES, PART A: RECOVERY, UTILIZATION, AND ENVIRONMENTAL EFFECTS
2026, VOL. 48, NO. 1, 2678537
https://doi.org/10.1080/15567036.2026.2678537

Taylor & Francis by informa

RESEARCH ARTICLE

Check for updates

Theoretical and experimental investigations of fixed-focus Fresnel-lens solar collectors with different cavity receivers

Vishwas Mahadeo Palve[a,b] and Gajanan Namdeorao Shelke[a,c]

[a]Department of Mechanical Engineering, MET's Institute of Engineering, (Savitribai Phule Pune University, Pune), Maharashtra, Bhujbal Knowledge City, Nashik, India; [b]Department of Mechanical Engineering, Vidyavardhini's College of Engineering and Technology, Mumbai, India; [c]Department of Mechanical Engineering, Sandip Institute of Engineering and Management, Sandip Foundation, Nashik, India

ABSTRACT

Although Fresnel lens solar collectors (FLSCs) with cavity receivers are extensively employed in low- and medium-temperature applications, the geometrical characteristics of the receiver exhibit significant effects on overall thermal performance. However, comparative experimental investigations of various cavity receiver geometries for FLSCs under real outdoor conditions remain limited. Hence, to optimize the cavity receiver design, the current study tested FLSC with various receiver geometries, including conical, spherical, and cylindrical. The fixed-focus FLSC with cavity receiver test rig was designed and tested in outdoor conditions of Mumbai, India. The optical-thermal model for an FLSC with cavity receivers is developed based on conjugate heat transfer between the receiver and surroundings. The model, validated with outdoor experimental measurements, was solved to predict heat removal factors (F_R) and feedwater outlet temperatures ($T_{f,o}$) for different receivers. The result showed that the conical receiver exhibited the lowest overall heat loss coefficient (U_L), resulting in the maximum $T_{f,o}$ and F_R of 58.52 °C and 0.66, followed by the spherical receiver (56.88 °C and 0.64) and the cylindrical receiver (55.29 °C and 0.62). Hence, the conical receiver was selected as the optimum geometry. Furthermore, it was found that solar intensity increased thermal losses ($\dot{Q}_{loss}$), while an increase in the mass flow rate of feedwater marginally influenced $\dot{Q}_{loss}$, useful heat transfer to feedwater, and $T_{f,o}$. Increasing coil length at constant diameter decreased $T_{f,o}$ due to a larger exposed area for thermal losses, resulting in an increased U_L.

ARTICLE HISTORY
Received 2 August 2025
Revised 7 May 2026
Accepted 15 May 2026

KEYWORDS
Cavity receiver; concentrated solar energy; fixed-focus; fresnel lens; solar

1. Introduction

Concentrating solar technologies (CST) have emerged as a viable solution for meeting heat demand in low, medium, and high-temperature applications in the domestic, agricultural, and industrial sectors (Zayed et al. 2021). Among the CST, Fresnel lenses are widely used in applications including water heating, solar desalination, solar cooking, solar lighting, and concentrated photovoltaics due to their lightweight, ease of manufacture, lower maintenance, and robust design. Solar collectors based on Fresnel lenses are categorized into line-focused and point-focused configurations. Line-focused Fresnel lens solar collectors (FLSCs) concentrate solar radiation along a linear focal line and are generally used with linear receivers for medium- to high-temperature applications. In contrast, point-focused FLSCs concentrate solar radiation to a small focal point, allowing the use of cavity receivers with different geometrical shapes, which enables the achievement of higher optical concentration ratios compared to line-focused configurations. The choice of FLSC configuration depends on the required thermal load, receiver design, and intended application. Due to the concentration of solar radiation over a small, well-defined focal area, point-focused configurations are primarily employed in high-flux applications, whereas line-focused configurations are mainly used in large-scale distributed solar thermal systems. The optical and thermal efficiencies of a FLSC are primarily determined by the receiver material and geometry (Zhai et al. 2010). Owing to lower thermal

CONTACT Gajanan Namdeorao Shelke gnshelke@gmail.com Department of Mechanical Engineering, Mumbai Educational Trust Institute of Engineering, Nashik 422003, India

and optical losses, cavity receivers are extensively employed in FLSCs. Effective insulation in the cavity receiver reduced conduction, convection, and radiation losses while increasing solar energy absorption.

Numerous studies have extensively investigated various geometries for Fresnel lens solar collectors. Le Quere, Penot, and Mirenayat (1981) conducted theoretical and experimental investigations on thermal heat losses from a cubical cavity receiver. In a similar study, Penot (1982) evaluated heat losses in a square open cavity receiver. Sharma et al. (2020) developed a numerical model to simulate the heat transfer characteristics of the helical cavity receiver in FSLC. The results revealed that, among the various geometrical characteristics of helical receivers, coil diameter exhibited a significant effect on thermal performance index. Furthermore, they observed that changing the flow direction from downward to upward reduced efficiency by about 12%. Le Roux, Bello-Ochende, and Meyer (2014) studied the effect of geometrical characteristics of a rectangular open-cavity receiver on the temperature profile and heat transfer rates. The result indicated that maximum thermal efficiency reached 75% with an open-cavity receiver. The numerical modelling and experimental investigation of air tube-cavity receiver is carried out by Qiu et al. (2015). The results revealed that while decreasing the inner radius to 4 mm increased thermal efficiency by about 8%, the pressure drop increased by 56 kPa. Loni et al. (2016) optimized the geometric characteristics of a cylindrical cavity receiver to improve thermal efficiency. The results indicated that smaller tube diameters and cavity depths increased thermal efficiency while increasing pressure drops. A recent study tested FLSCs with square (Jensen et al. 2022) and rectangular (González-Camarillo et al. 2024) shaped receivers to improve thermal performance. Xie, Dai, and Wang (2013) tested a line-focused FLSC with eight different cavity receivers and observed that the triangular cavity receiver exhibited the highest heat removal factor.

Lin et al. (2014) found that for a line-focused FLSC, a triangular-shaped receiver outperformed other arc, semicircle, and rectangle-shaped receivers. Wang et al. (2019) investigated the effect of receiver geometry parameters on the performance of fixed-focus FLSC in solar cooking. Conical, spherical, and cylindrical cavity receivers were integrated with a reflected cone at the bottom. The results showed that the cone angle and reflectivity of the bottom reflective cone increased energy absorptivity in all of the tested cavity receivers; however, heat flux uniformity decreased. Furthermore, adding a reflective cone to the bottom increased the optical efficiency of the conical cavity receiver by about 36.46%, followed by spherical (3.74%) and conical cavity receivers (1.79%). The effect of the location of different cavity receivers on the optical and thermal performance was investigated by Daabo, Mahmoud, and Al-Dadah (2016). They observed that heat flux on the receiver tip area is independent of receiver position.

Reddy, Vikram, and Veershetty (2015) carried out numerical simulations of a hemispherical cavity receiver to estimate convection and radiation heat losses. The simulated results showed that in the sideward-facing receiver position, natural convection heat loss was highest while forced convection heat loss was lowest, and vice versa in the downward-facing receiver position. Furthermore, receiver inclination, diameter ratio, and wind speed significantly affect the heat losses. At higher wind speeds, forced convection contributes more to total heat losses. Prakash, Kedare, and Nayak (2012) estimated the convection heat loss from three different receivers: cubical, spherical, and hemispherical. The simulations were performed for various inclinations and receiver opening ratios, and the results showed that stagnation and convection zones reduced convection loss in all tested cavities. Jilte, Kedare, and Nayak (2014) conducted CFD simulations of conical, cylindrical, and various combined conical and cylindrical cavities for convective losses in wind and no-wind conditions. The results showed that for different inclinations and mouth blockage areas, the conical cavity receiver exhibited the lowest convection heat loss compared to other cavity geometries.

Based on the existing literature, FLSCs with cavity receivers have been extensively investigated for low- and medium-temperature thermal applications. Most previous studies have primarily focused on line-focused FLSC configurations, employing various receiver geometries such as cubical, helical, cylindrical, triangular, spherical, and conical shapes, mainly through numerical simulations and limited experimental validation. However, systematic experimental investigations on point-focused FLSCs incorporating different cavity receiver geometries remain scarcely reported in open literature. The optical characteristics and geometrical configuration of the receiver play a critical role in determining the overall thermal efficiency of FLSCs, thereby necessitating the development of combined optical-thermal performance models for different receiver designs. The novelty of this study lies in the combined experimental and thermo-optical evaluation, under real outdoor conditions, of multiple cavity receiver geometries in a point-focused FLSC to systematically investigate the influence of receiver geometry on optical interception, thermal losses, and overall collector performance. In the present work, a point-focused FLSC test rig equipped with interchangeable cavity receivers is designed and experimentally evaluated under real outdoor operating conditions. A comparative performance evaluation of three cavity receiver geometries including conical, spherical, and cylindrical is carried out under outdoor conditions. Although various receiver geometries, including cubical, helical, triangular, and other complex numerically optimized shapes, have been reported in the literature, these geometries often pose challenges in terms of fabrication complexity and ease of interchangeability in experimental setups, thereby limiting their suitability for controlled performance comparison. In contrast, due to their geometrical simplicity, ease of fabrication, symmetrical optical interception characteristics, and well-defined heat-transfer surfaces, conical, spherical, and cylindrical cavity receivers represent fundamental and widely adopted baseline geometries in point-focused FLSCs. These basic cavity shapes exhibit distinct optical interception behavior and thermal loss mechanisms, making them suitable candidates for a controlled and systematic experimental comparison. Therefore, the aim of this work is to investigate the effect of cavity receiver geometry on the thermal performance of a fixed-focus FLSC. The objectives are: (i) to experimentally evaluate different cavity geometries under outdoor conditions, (ii) to develop and validate an optical-thermal model, and (iii) to determine the optimum receiver configuration based on thermal performance indicators, and (iv) investigate the effects of solar irradiance, feedwater mass flow rate, and receiver length on the overall heat transfer coefficient, heat removal factor, and feedwater outlet temperature.

2. Experimental setup

The experimental setup of an FLSC with various receiver geometries is installed on the rooftop of the solar energy laboratory at VCET in Mumbai, India. Figures 1 and 2 show a schematic diagram and an actual photograph of the experimental setup. The test setup comprised primarily of a Fresnel lens (FL), cavity, receiver, and storage tank. A portion of solar energy incident on the Fresnel lens is reflected, while the remainder is refracted through the lens and focused on the receiver surface. The heat transfer fluid (HTF) circulated through the receiver, absorbing heat and increasing temperature. The cavity is thermally insulated to reduce heat loss to the surroundings. The FL is 2 m in length and 1 m in width and is made of 3 mm thick acrylic. The FL is mounted on an aluminum frame and installed in a North–South direction. The FLSC is tracked on a single axis (East–West) using a 12V DC motor integrated with the L293DNE microcontroller. Table 1 lists the detailed specifications of the FLSC. Optimal receiver geometry

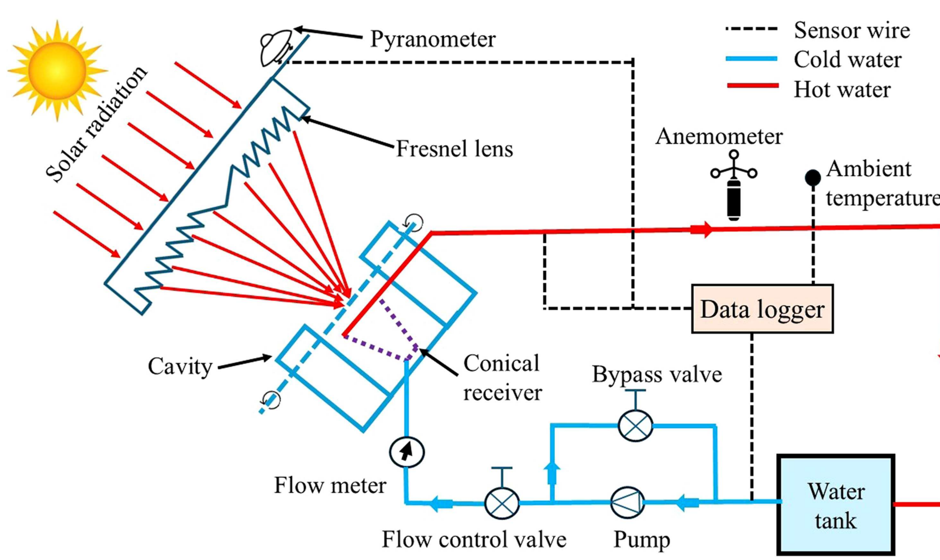

Figure 1. Schematic of the experimental setup of a FLSC with different receiver geometries.

Figure 2. Actual photograph of the experimental setup.

Table 1. Detailed specifications of FLSC.

Specification	Value	Unit
Optical efficiency (η_{opt})	0.85	
absorptive factor (α_f)	0.85	
Absorptivity cavity wall surface (α_c)	0.98	
Emissivity of cavity wall surface (ε_{cv})	0.85	
Length (L_{sc})	2	m
Width (W_{sc})	1	m
Focal length	10	cm
Cavity inside diameter ($D_{cv,i}$)	0.20	m
Optical concentration ratio (C_o)	161	
Cavity outside diameter ($D_{cv,o}$)	0.22	m
Receiver coil outside diameter ($D_{cr,o}$, $D_{sr,o}$, $D_{clr,o}$)	0.0062	m
Receiver coil inside diameter ($D_{cr,i}$, $D_{sr,i}$, $D_{clr,i}$)	0.006	m
Receiver coil length (L_{cr}, L_{sr}, L_{clr})	1, 1.22, 1.41	m
Thermal conductivity of cavity material (k_{cv})	385	W/m^2 K
Depth of cavity (d_{cv})	0.15	m
Thermal conductivity of receiver material (k_{cr}, k_{sr}, k_{clr})	385	W/m^2 K
Thermal conductivity of insulation material (k_{ins})	45	W/m^2 K
Insulation material thickness (t_{ins})		
Cavity tilt angle (θ_{cv})	19	°

improves optical efficiency by increasing solar energy absorption and enabling efficient heat transfer to the working fluid, thereby increasing overall thermal efficiency. To optimize receiver geometry for point-focused FLSC, three different receiver shapes, including cylindrical, spherical, and conical, are tested in the current study. Receivers are made of copper, and Figure 3 depicts schematic representations and actual photographs of three different receiver geometries. In the test setup, 187W centrifugal pumps circulate HTF through the receiver. Findings of Ref. (Sharma et al. 2020) revealed that for cavity receivers, downward flow showed a higher thermal efficiency than upward flow; thus, in the current study, downward flow was maintained during the testing of all cavity receivers. The storage tank and cavity were insulated with 4-mm fiberglass insulation.

Figure 3. Schematic and actual photographs of cylindrical, conical, and spherical receivers.

The wind speed is measured using an AM-4201 digital anemometer (±3% accuracy). The HTF flow rate is measured using electromagnetic flowmeters with a range of 0–5 kg/min (accuracy ± 3%). The solar radiation incident on the Fresnel lens was measured using a pyranometer (LP PYRA 03) with a range of 0–2000 W/m^2 and an accuracy of 1 W/m^2. In the test setup, air and water temperature are measured using a K-type thermocouple (±0.2 °C accuracy) connected to an 8-channel data logger. All measurements were taken during 1-h intervals.

The experimentally measured values of wind speed, solar irradiance, HTF flow rate, and air and water temperatures were subsequently used in the thermo-optical and thermal performance calculations.

The uncertainty of the instrument (u_m) depends on its accuracy (a_m) and can be calculated using the following equation (Lawal et al. 2020):

$$u_m = \frac{a_m}{\sqrt{3}}. \tag{1}$$

The uncertainty in the calculated parameter (δ_R) is evaluated based on the u_m and mathematically expressed as follows (Lawal et al. 2020):

$$\delta_R = \left[\left(\frac{\partial R}{\partial x_1}\delta_1\right)^2 + \left(\frac{\partial R}{\partial x_2}\delta_2\right)^2 + \cdots\cdots\cdots\cdots\cdots\cdots + \left(\frac{\partial R}{\partial x_n}\delta_n\right)^2\right]^{1/2}. \tag{2}$$

The uncertainty in the calculated parameter of the heat removal factor was found to be 2.88%.

3. Mathematical modeling

To model the FLSC, the following assumptions are employed:

- The Fresnel lens is free of fabrication errors and all refracted rays are focused on the receiver.

- The axial directional temperature variation is ignored (Perini et al. 2017).
- The thermal flux is uniform in the cavity and along the receiver surface.
- The conduction heat transfer through receiver wall surface is neglected (Mokhtar, Boussad, and Noureddine 2016).
- Loss of energy due to tracking errors are ignored (Perini et al. 2017).

3.1 Fresnel lens and cavity

The solar energy concentrated by the Fresnel lens ($\dot{Q}_{\text{in}}$) into a cavity is given by (Banakar et al. 2017):

$$\dot{Q}_{\text{in}} = \eta_{\text{opt}}\, \alpha_f G_T A_{\text{sc}} C_o. \tag{3}$$

where A_{sc} is the collector area, η_{opt} is the optical efficiency of FL, α_f is the absorptive factor, G_T is the global solar radiation on the FL, and C_o is the optical concentration ratio.

The solar energy absorbed by a cavity ($\dot{Q}_{\text{in,cv}}$) depends on the absorptivity of the wall surface (α_c) and is mathematically expressed as follows (Shen et al. 2017):

$$\dot{Q}_{\text{in,cv}} = \frac{\alpha_c}{1 - (1 - \alpha_c)\left(1 - \frac{A_{\text{sc}}}{A_{\text{cv},i}}\right)} \dot{Q}_{\text{in}}. \tag{4}$$

where $A_{\text{cv},i}$ is the inner surface area of the cavity.

Figure 4 illustrates the thermal resistance network for FLSC. The useful energy transfer to the HTF, $\dot{Q}_u$, is calculated by Banakar et al. (2017); Xie, Dai, and Wang (2011):

$$\dot{Q}_u = \dot{Q}_{\text{in,cv}} - \dot{Q}_{\text{loss}}. \tag{5}$$

where $\dot{Q}_{\text{loss}}$ is the total solar energy loss from the cavity, combining conduction ($\dot{Q}_{\text{cond}}$), convection ($\dot{Q}_{\text{conv}}$), and radiation ($\dot{Q}_{\text{rad}}$) heat losses.
$\dot{Q}_{\text{loss}}$ is given by:

$$\dot{Q}_{\text{loss}} = \dot{Q}_{\text{cond}} + \dot{Q}_{\text{conv}} + \dot{Q}_{\text{rad}}. \tag{6}$$

$\dot{Q}_{\text{cond}}$ is calculated by (Cengel and Ghajar 2007):

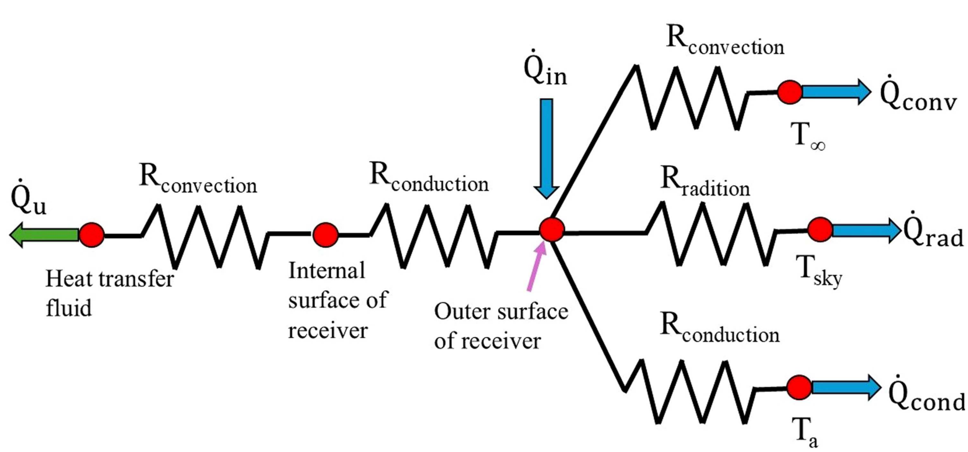

Figure 4. Thermal resistance network for FLSC.

$$\dot{Q}_{\text{cond}} = \frac{(T_{\text{cv}} - T_a)}{\frac{\ln\left(\frac{D_{\text{cv},o}}{D_{\text{cv},i}}\right)}{2\pi k_{\text{cv}} d_{\text{cv}}} + \frac{\ln\left(\frac{D_{\text{cv},o} + t_{\text{ins}}}{D_{\text{cv},o}}\right)}{2\pi k_{\text{ins}} d_{\text{cv}}} + \frac{1}{h_a A_{\text{cv},o}}}. \tag{7}$$

where T_{cv} and T_a are cavity and ambient temperatures, $D_{\text{cv},o}$ and $D_{\text{cv,in}}$ are the cavity outside and inside diameters, d_{cv} is the depth of the cavity, k_{cv} is the thermal conductivity of the cavity material, t_{ins} and k_{ins} are the insulation material thickness and thermal conductivity, $A_{\text{cv},o}$ is the outside surface area of the cavity, and h_a is the convective heat transfer coefficient (HTC) due to airflow over the cavity.

h_a is the function of heat transfer coefficients due to natural ($h_{a,\text{nat}}$) and forced ($h_{a,\text{for}}$) convection of airflow, and it is mathematically expressed as follows (Ruelas, Velázquez, and Cerezo 2013):

$$h_a = (h_{a,\text{nat}}{}^3 - h_{a,\text{for}}{}^3)^{1/3}. \tag{8}$$

$h_{a,\text{nat}}$ and $h_{a,\text{for}}$ are calculated using the following correlations based on Reynolds number (Re_a), Prandtl numbers (Pr_a), and Rayleigh number (Ra_a) of air (Ruelas, Velázquez, and Cerezo 2013).

$$h_{a,\text{nat}} = (0.27\text{Ra}_a{}^{1/4})\frac{k_a}{D_{\text{cv},o}} \cdots\cdots\cdots\cdots (10^3 \le \text{Ra} \le 10^6), \tag{9}$$

$$h_{a,\text{for}} = (0.66\,\text{Re}_a{}^{1/2}\,\text{Pr}_a{}^{1/3})\frac{k_a}{D_{\text{cv},o}}. \tag{10}$$

where k_a is the thermal conductivity of ambient air.

$\dot{Q}_{\text{conv}}$ is calculated from the following equation (Aboelmaaref et al. 2023):

$$\dot{Q}_{\text{conv}} = A_{\text{cv},i}(T_{cv} - T_a)(h_{\text{conv,nat}} + h_{\text{conv,for}}), \tag{11}$$

where $h_{\text{conv,nat}}$ and $h_{\text{conv,for}}$ are natural and forced convective HTCs of air inside the cavity.

$h_{\text{conv,nat}}$ is calculated from the following correlation (Aboelmaaref et al. 2023):

$$h_{\text{conv,nat}} = 0.\,088 D_{r,o} k_r \text{Gr}_a{}^{1/3}\left(\frac{T_{\text{cv}}}{T_a}\right)^{0.18}(\cos\theta_{\text{cv}})^{2.47}\left(\frac{D_{r,o}}{D_{\text{cv},o}}\right)^m, \tag{12}$$

$$m = -0.982\left(\frac{D_{r,o}}{D_{\text{cv},i}}\right) + 1.12. \tag{13}$$

where $D_{r,o}$ and k_r are the outside diameter and thermal conductivity of the receiver, Gr_a is the Grashof number, and θ_{cv} is the cavity tilt angle.

$h_{\text{conv,for}}$ is calculated by (Mendoza Castellanos et al. 2017):

$$h_{\text{conv,for}} = f(\theta_{\text{cv}})\,V_w{}^{1.401}, \tag{14}$$

$$f(\theta_{\text{cv}}) = 0.1634 + 0.7498\sin(\theta_{\text{cv}}) + 0.5026\sin(2\theta_{\text{cv}}) + 0.3278\sin(\theta_{\text{cv}}). \tag{15}$$

where V_w is the wind speed.

$\dot{Q}_{\text{rad}}$ is calculated from the following equation (Al-Dafaie, Dahdolan, and Al-Nimr 2016; Mendoza Castellanos et al. 2017; Ruelas, Velázquez, and Cerezo 2013):

$$\dot{Q}_{\text{rad}} = (1 - \alpha_{c,\text{eff}})\dot{Q}_{\text{in}} + \sigma\varepsilon_{\text{cv}} A_{\text{cv},i}(T_{\text{cv}}{}^4 - T_a{}^4), \tag{16}$$

where $\alpha_{c,\text{eff}}$ and ε_{cv} are the effective absorptivity and emissivity of the cavity wall surface, and σ is the Stefan–Boltzmann constant.

$\alpha_{c,\text{eff}}$ can be expressed as follows (Mendoza Castellanos et al. 2017):

$$\alpha_{c,\text{eff}} = \frac{\alpha_c}{\alpha_c + (1 - \alpha_c)\frac{A_{sc}}{A_{cv,i}}}. \tag{17}$$

The overall heat loss coefficient (HLC) for the cavity, U_L, is calculated as follows (Duffie and Beckman 2002):

$$\dot{Q}_{\text{loss}} = U_L A_{cv,i}(T_{cv} - T_a). \tag{18}$$

3.2 Conical receiver (CR)

The useful energy transfer to circulating fluid in CR, $\dot{Q}_{u,\text{cr}}$, is given by:

$$\dot{Q}_{u,\text{cr}} = A_r[S - U_{L,\text{cr}}(T_{cr} - T_a), \tag{19}$$

$$S = \eta_{\text{opt}} G_T C_o \sin\frac{\theta}{2}, \tag{20}$$

where A_r is the receiver coil outside surface area, S is the energy absorbed by the FL per unit receiver coil outside surface area, $U_{L,\text{cr}}$ and T_{cr} are the HLC and average temperature of CR, and θ is the vertex angle of the cross section.

$\dot{Q}_{u,\text{cr}}$ can also be expressed as (Cengel and Ghajar 2007):

$$\dot{Q}_{u,\text{cr}} = \frac{(T_{\text{cr}} - T_{f,m})}{\frac{1}{\pi D_{\text{cr},i} L_{\text{cr}} h_f} + \frac{1}{2\pi k_{\text{cr}} L_{\text{cr}}} ln\left(\frac{D_{\text{cr},o}}{D_{\text{cr},i}}\right)}, \tag{21}$$

$$L_{\text{cr}} = \frac{\pi D_{\text{cr}}(D_{\text{cr},o} + D_r)}{4D_{cr,o}\sin\frac{\theta}{2}}. \tag{22}$$

where $D_{\text{cr},o}$ and $D_{\text{cr},i}$ are outside and inside diameters of the CR coil, L_{cr} and k_{cr} are the length and thermal conductivity of the CR coil, D_r is the diameter of the cavity receiver, and h_f and $T_{f,m}$ are the convective HTC and average temperature of the circulating fluid.

$T_{f,m}$ is calculated by:

$$T_{f,m} = \frac{T_{f,i} + T_{f,o}}{2}. \tag{23}$$

where $T_{f,i}$ and $T_{f,o}$ are inlet and outlet temperatures of circulating fluid.

h_f for laminar flow in the receiver is calculated from the following Nusselt number (Nu) correlation (Shaikh and Ismail 2023):

$$\text{Nu} = \frac{h_f D_{\text{cr},i}}{k_f} = \left[\frac{\sqrt{D_n}}{Z}\right], \tag{24}$$

$$D_n = \text{Re}_f\sqrt{\frac{D_{\text{cr},i}}{D_{\text{turn}}}}, \tag{25}$$

$$Z = \frac{2}{11}\left(1 + \sqrt{1 + \frac{77}{4}\text{Pr}_f{}^2}\right), \tag{26}$$

$$\text{Re}_f = \frac{4\dot{m}_f}{\pi\mu_{fD_{\text{cr},i}}}, \tag{27}$$

$$\mathrm{Pr}_f = \frac{\mu_f C_p}{k_f}. \tag{28}$$

where $\dot{m}_f$, k_f, C_p, μ_f, Re_f, and Pr_f are the mass flow rate, thermal conductivity, specific heat, dynamic viscosity, Reynolds number, and Prandtl number of circulating fluids, respectively, and D_{turn} is the receiver coil turn diameter.

h_f for turbulent flow is calculated by (Garg, Das, and Tyagi 2022):

$$\mathrm{Nu} = \frac{h_f D_{\text{cr},i}}{k_f} = \frac{\frac{f}{8}(\mathrm{Re_f} - 1000)\mathrm{Pr}_f}{1 + 12.7\sqrt{f/8}\quad [\mathrm{Pr}_f^{2/3} - 1]} \ldots\ldots\ldots\ldots \begin{matrix} 0.5 \le \mathrm{Pr}_f \le 2000 \\ 3 \times 10^6 \le \mathrm{Re}_f \le 5 \times 10^6 \end{matrix}, \tag{29}$$

$$f = (1.82 \log_{10}(\mathrm{Re}_f) - 1.64)^{-2}. \tag{30}$$

T_{cr} from Eq. (21) is substituted in Eq. (19) and solved, yielding the following equation (Xie et al., n.d.) :

$$\dot{Q}_{u,\text{cr}} = \frac{S - U_{L,\text{cr}}(T_{f,m} - T_a)}{\frac{4}{\pi D_r^2} + \frac{4D_{\text{cr},o}\sin\frac{\theta}{2}}{\pi D_r(D_{\text{cr},o} + D_r)}\left(\frac{1}{\pi D_{\text{cr},i} L_{\text{cr}} h_f} + \frac{1}{2\pi k_{\text{cr}} L_{\text{cr}}} \ln\left(\frac{D_{\text{cr},o}}{D_{\text{cr},i}}\right)\right) U_{L,\text{cr}}} = D_{\text{cr}} F_{\text{cr}}'(\eta_{\text{opt}} G_T - U_L (T_{f,m} - T_a)), \tag{31}$$

where,

$$F_{\text{cr}}' = \frac{1/D_r}{\frac{4}{C_o \pi D_r^2} + \frac{4D_{\text{cr},o}\sin\frac{\theta}{2}}{\pi \mathrm{D_r}(D_{\text{cr},o} + D_{\text{cr}})}\left(\frac{1}{\pi D_{\text{cr},i} L_{\text{cr}} h_f} + \frac{1}{2\pi k_{\text{cr}} L_{\text{cr}}} \ln\left(\frac{D_{\text{cr},o}}{D_{\text{cr},i}}\right)\right) U_L}, \tag{32}$$

$$U_{L,\text{cr}} = U_L C_o \sin\frac{\theta}{2}. \tag{33}$$

The collector heat removal factor ($F_{R,\text{cr}}$) and $T_{f,o}$ in CR are calculated from the following equations (Xie, Dai, and Wang 2011):

$$F_{R,\text{cr}} = \frac{4\dot{m}_f C_p}{\pi D_r^2 U_L C_o \sin\frac{\theta}{2}}\left[1 - \exp\left(-\frac{\pi D_r^2 U_L F_{\text{cr}}'(D_{\text{cr},o} + D_r)}{4\dot{m}_f C_p \sin\frac{\theta}{2} D_{\text{cr}}}\right)\right], \tag{34}$$

$$\dot{Q}_{u,\text{cr}} = A_r F_{R,\text{cr}} C_o \sin\frac{\theta}{2}[\eta_{\text{opt}} G_T - U_L(T_{f,i} - T_a) = \dot{m}_f C_p (T_{f,o} - T_{f,i}). \tag{35}$$

3.3 Spherical receiver (SR)

The useful energy transfer to HTF in SR, $\dot{Q}_{u,\text{sr}}$, is given by (Xie, Dai, and Wang 2011):

$$\dot{Q}_{u,\text{sr}} = \frac{S - U_{L,\text{sr}}(T_{f,m} - T_a)}{\frac{4}{\pi D_r^2} + \frac{1}{L_{sr}}\left(\frac{1}{\pi D_{\text{sr},i} h_f} + \frac{1}{2\pi k_{\text{sr}}} ln\left(\frac{D_{\text{sr},o}}{D_{\text{sr},i}}\right)\right) U_{L,\text{sr}}} = D_r F_{\text{sr}}'(\eta_{\text{opt}} G_T - U_L (T_{f,m} - T_a)), \tag{36}$$

$$U_{L,\text{sr}} = \frac{U_L C_o \sin^2\left(\frac{\theta}{2}\right)}{2\left(1 + \cos\left(\frac{\theta}{2}\right)\right)}, \tag{37}$$

$$L_{\mathrm{sr}} = \frac{\pi D_r \sin\frac{\theta}{2}(2\pi D_{\mathrm{sr},o} - \theta D_{\mathrm{sr},o} - \theta D_r) + 2\pi^2 D_r^2}{8D_{\mathrm{sr},o}\sin^2\left(\frac{\theta}{2}\right)}, \tag{38}$$

$$F_{\mathrm{sr}}' = \frac{1/D_r}{\frac{8\left(1+\cos\left(\frac{\theta}{2}\right)\right)}{C_o\pi D_r^2\sin^2\left(\frac{\theta}{2}\right)} + \frac{1}{L_{\mathrm{sr}}}\left(\frac{1}{\pi D_{\mathrm{sr},i}h_f} + \frac{1}{2\pi k_{\mathrm{sr}}}\ln\left(\frac{D_{\mathrm{sr},o}}{D_{\mathrm{sr},i}}\right)\right)U_L}. \tag{39}$$

where $D_{\mathrm{sr},o}$, $D_{\mathrm{sr},i}$, L_{sr}, and k_{sr} are the outside diameter, inside diameter, length, and thermal conductivity of an SR coil, and $U_{L,\mathrm{sr}}$ is the HLC of SR.

The collector heat removal factor ($F_{R,\mathrm{sr}}$) and $T_{f,o}$ in SR are calculated from the following equations (Xie, Dai, and Wang 2011):

$$F_{R,\mathrm{sr}} = \frac{8\left(1+\cos\left(\frac{\theta}{2}\right)\right)\dot{m}_f C_p}{U_L C_o \pi D_r^2 \sin^2\left(\frac{\theta}{2}\right)}\left[1 - \exp\left(-\frac{L_{\mathrm{sr}} U_L F_{\mathrm{sr}}' D_r)}{\dot{m}_f C_p}\right)\right], \tag{40}$$

$$\dot{Q}_{u,\mathrm{sr}} = A_r F_{R,\mathrm{sr}} \frac{C_o \sin^2\left(\frac{\theta}{2}\right)}{2(1+\cos\left(\frac{\theta}{2}\right)}[\eta_{\mathrm{opt}} G_T - U_L(T_{f,i} - T_a) = \dot{m}_f C_p(T_{f,o} - T_{f,i}). \tag{41}$$

3.4 Cylindrical receiver (CLR)

The useful energy transfer in CLR, $\dot{Q}_{u,\mathrm{clr}}$, is given by (Xie, Dai, and Wang 2011):

$$\dot{Q}_{u,\mathrm{clr}} = \frac{S - U_{L,\mathrm{clr}}(T_{f,m} - T_a)}{\frac{4}{\pi D_r^2} + \frac{D_{\mathrm{clr},o}}{\pi D_r L_{\mathrm{clr}}}\left(\frac{1}{\pi D_{\mathrm{clr},i}h_f} + \frac{1}{2\pi k_{\mathrm{clr}}} ln\left(\frac{D_{\mathrm{clr},o}}{D_{\mathrm{clr},i}}\right)\right)U_{L,\mathrm{clr}}} = D_r F_{\mathrm{clr}}'(\eta_{\mathrm{opt}} G_T - U_L(T_{f,m} - T_a), \tag{42}$$

$$U_{L,\mathrm{clr}} = \frac{U_L C_o D_r}{4L_{\mathrm{clr}}}, \tag{43}$$

$$F_{\mathrm{clr}}' = \frac{1/D_r}{\frac{16L_{\mathrm{clr}}}{C_o\pi D_r^3} + \frac{D_{\mathrm{clr},o}}{\pi D_r L_{\mathrm{clr}}}\left(\frac{1}{\pi D_{\mathrm{clr},i}h_f} + \frac{1}{2\pi k_{\mathrm{clr}}} ln\left(\frac{D_{\mathrm{clr},o}}{D_{\mathrm{clr},i}}\right)\right)U_L}. \tag{44}$$

where $D_{\mathrm{clr},o}$, $D_{\mathrm{clr},i}$, L_{clr}, and k_{clr} are the outside diameter, inside diameter, length, and thermal conductivity of an CLR coil, and $U_{L,\mathrm{clr}}$ is the HLC of CLR.

The collector heat removal factor ($F_{R,\mathrm{clr}}$) and $T_{f,o}$ in CLR are calculated from following equations (Xie, Dai, and Wang 2011):

$$F_{R,\mathrm{clr}} = \frac{16L_{\mathrm{clr}}\dot{m}_f C_p}{U_L C_o \pi D_r^2}\left[1 - \exp\left(-\frac{F_{\mathrm{clr}}' U_L \pi D_r^2 L_{\mathrm{clr}})}{\dot{m}_f C_p D_{\mathrm{clr},o}}\right)\right], \tag{45}$$

$$\dot{Q}_{u,\mathrm{clr}} = A_r F_{R,\mathrm{clr}} \frac{C_o D_r}{4L_{\mathrm{clr}}}[\eta_{\mathrm{opt}} G_T - U_L(T_{f,i} - T_a) = \dot{m}_f C_p(T_{f,o} - T_{f,i}). \tag{46}$$

The zero-dimensional thermal-optical model for a FLSC with different receiver shapes was solved using a computer simulation program developed in MATLAB. The model simulates the fluid outlet temperature from the conical, spherical, and cylindrical receivers using the geometrical and optical parameters of the FLSC and meteorological data.

4. Results and discussion

To assess performance, a series of experimental tests were carried out on the FLSC with various receiver geometries (CR, SR, and CLR) under real-world meteorological conditions. The experiments were conducted during clear summer days in February and March 2025, with measurements recorded from 09:00 to 17:00 h. In the tests, city tap water is used directly as HTF, and thermal properties influenced by contamination/salinity are not considered since there is no significant effect on water outlet temperatures in FLSC (Kabeel and Abdelgaied 2018). This section includes FLSC model validation, followed by a comprehensive parametric investigation to study the effects of receiver shapes, receiver length, HTF flow rate, and solar radiation.

4.1 Model validation

To assess the reliability of the developed thermo-optical model for an FLSC with different receiver shapes, numerically simulated water outlet temperatures ($T_{f,o}$) from CR, SR, and CLR were compared to experimental measurements. The HTF outlet temperature is a significant performance metric for the FLSC; hence, simulated $T_{f,o}$ is validated with experimental test results. Figure 5 depicts the statistical validation of $T_{f,o}$ from conical, spherical, and cylindrical receivers. The validation parameters exhibit comparable trends to the experimental test data. It is noticed from Figure 5 that the FLSC model predicted $T_{f,o}$ for different receiver shapes with a maximum deviation of 6%. This deviation is primarily due to the assumption of perfect tracking and uniform flux in the cavity. Based on Figure 5, the FLSC model with various receiver shapes is accurate enough to be used in further investigations.

4.2 Effect of solar radiation (G_T)

Figure 6 depicts the diurnal variations in G_T, ambient temperature (T_a), and wind velocity (V_w) on selected days. It can be seen from the figure that test days 15/2/2025 and 20/2/2025 were sunny, with clear skies and a daily average G_T of 707 W/m^2 and 688 W/m^2, respectively (varying within 3%). On 17/2/2025, the climate was cloudy, with a daily average G_T of 600 W/m², around 18% lower than on 15/2/2025. During all test days, T_a and V_w ranged from 28.01 to 35.91 °C and 0.4 m/s to 1.5 m/s, respectively, with no significant variation observed. The G_T peaked at noon (12.00–14.00), exceeding 750 W/m^2, but decreased to below 400 W/m^2 after 16.00.

Figure 7 illustrates the diurnal variation of concentrated solar energy in the cavity ($\dot{Q}_{\text{in}}$), total energy loss from the cavity ($\dot{Q}_{\text{loss}}$), and useful energy transfer to the HTF ($\dot{Q}_u$). $\dot{Q}_{\text{in}}$ is higher on 15/2/2025 and 20/5/2025 than on 17/2/2025 due to more availability of G_T. The increased $\dot{Q}_{\text{in}}$ improved the cavity temperature, resulting in higher cavity losses (conduction, convection, and radiation). The $\dot{Q}_{\text{loss}}$on 15/2/2025 and 20/5/2025 are about 25% and 21% higher than on 17/2/2025, respectively, due to the higher cavity temperature

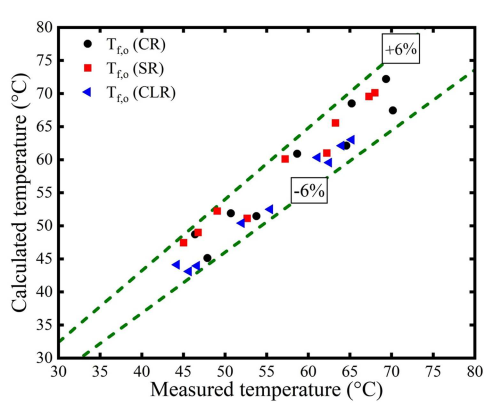

Figure 5. Comparison of measured and calculated water outlet temperature from CR, SR, and CLR.

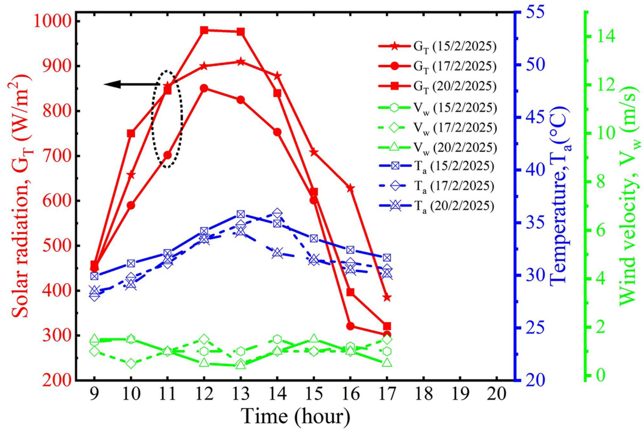

Figure 6. Diurnal variation of solar radiation (G_T), ambient temperature (T_a), and wind velocity (V_w) during outdoor testing.

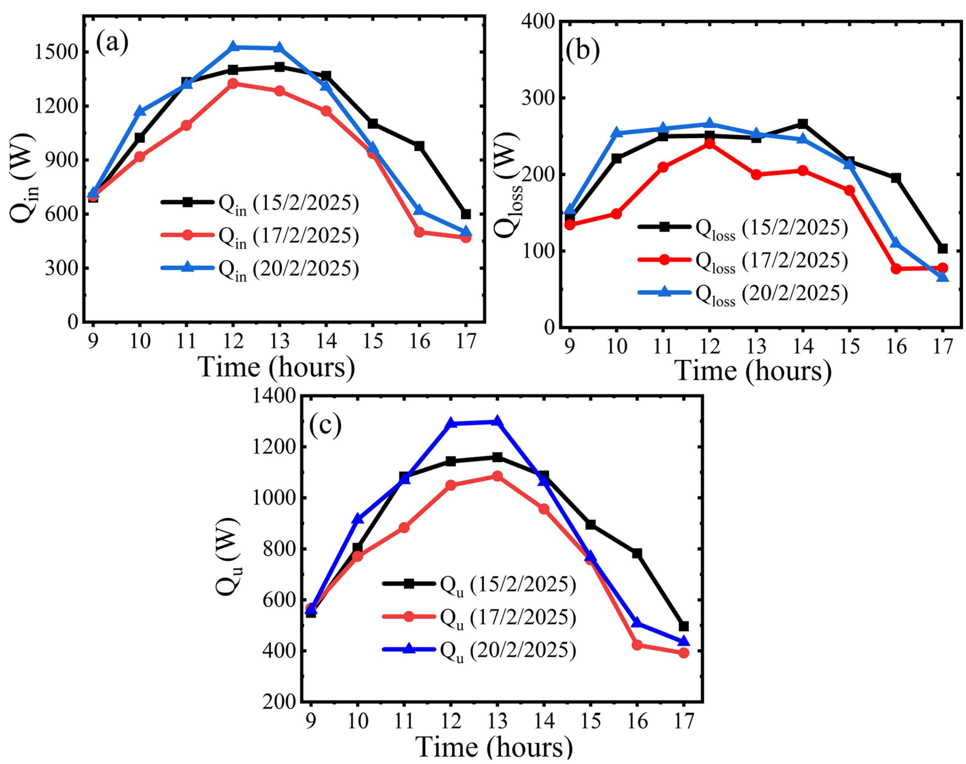

Figure 7. Diurnal variation of (a) concentrated solar energy inside cavity ($\dot{Q}_{\text{in}}$), (b) cavity heat loss ($\dot{Q}_{\text{loss}}$), and (c) useful heat transfer to HTF ($\dot{Q}_u$) during outdoor testing.

reached. Due to the limited availability of G_T, the $\dot{Q}_u$ is significantly lower on 17/2/2025. Furthermore, $\dot{Q}_{\text{in}}$, $\dot{Q}_{\text{loss}}$, and $\dot{Q}_u$ are directly dependent on G_T; thus, they follow the same trend as G_T (lower in the morning and afternoon hours and peaking at noon). Figure 8 shows the hourly variation of $T_{f,o}$ during test days. The figure indicates that the trend of the $T_{f,o}$ is nearly parabolic, increasing with time of day, peaking at noon, and gradually decreasing in afternoon hours, following the same trend as G_T. The daily average $T_{f,o}$ on 15/2/2025 and 20/5/2025 reached 54.11 °C and 52.51 °C, respectively, which is about 6–8.5% higher than on 17/2/2025. This is attributed to higher availability of G_T, resulting in increased $\dot{Q}_{\text{in}}$ and $\dot{Q}_u$.

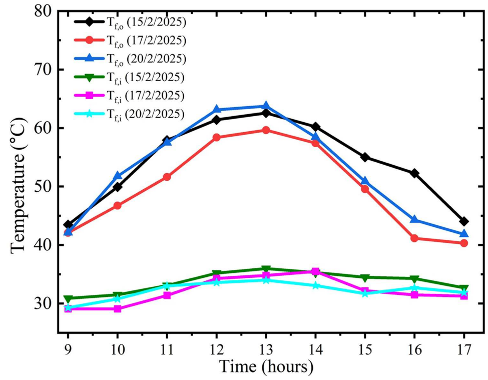

Figure 8. Diurnal variation of water inlet temperature ($T_{f,i}$) and water outlet temperature ($T_{f,o}$) during outdoor testing.

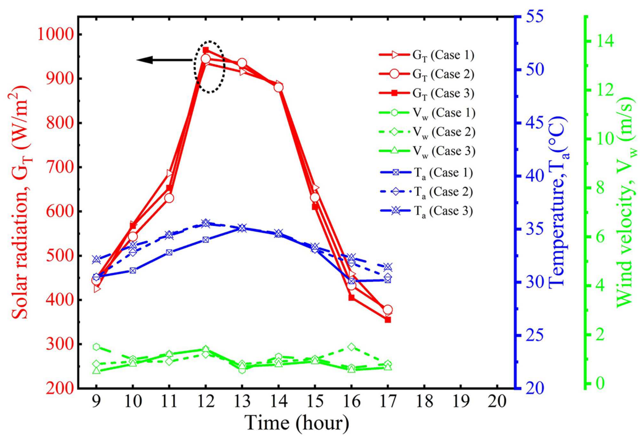

Figure 9. Diurnal variation of solar radiation (G_T), ambient temperature (T_a), and wind velocity (V_w) during outdoor experiments with various feedwater flow rates.

4.3 Effect of HTF flow rate ($\dot{m}_f$)

Figure 9 depicts the diurnal variation in G_T, and it can be seen that the test days were sunny, with day average G_T varying within 2%. Three experimental cases were considered: Case 1 ($\dot{m}_f$ = 0.5 kg/min), Case 2 ($\dot{m}_f$ = 1 kg/min), and Case 3 ($\dot{m}_f$ = 1.5 kg/min). The T_a and V_w varied from 30.11 °C to 35.61 °C and 0.5 m/s to 1.5 m/s, respectively. Figures 10 and 11 illustrate the diurnal variation of heat transfer rates ($\dot{Q}_{\text{in}}$, $\dot{Q}_{\text{loss}}$, & $\dot{Q}_u$) and $T_{f,o}$ for different $\dot{m}_f$in the receiver. Table 2 depicts the average $T_{f,o}$ for various $\dot{m}_f$. Figure 10(a–c) indicates that the $\dot{m}_f$ has no significant effect on $\dot{Q}_{\text{in}}$, $\dot{Q}_{\text{loss}}$, & $\dot{Q}_u$. Table 2 reveals that $\dot{Q}_{\text{loss}}$, & $\dot{Q}_u$ varied within 4.5% in all cases. This is due to the fact that the overall heat loss coefficient for the cavity, U_L, is marginally affected by increasing $\dot{m}_f$, resulting in no significant variation in $\dot{Q}_{\text{loss}}$, & $\dot{Q}_u$. Despite $\dot{Q}_u$ being constant in all cases, increasing $\dot{m}_f$ lowers $T_{f,o}$. The Reynolds numbers for $\dot{m}_f$of 0.5 kg/min, 1 kg/min, and 1.5 kg/min were about 1990, 3950, and 5950, respectively, indicating that the flow regime in the receiver is transitioning from laminar to turbulent. This results in a thinner thermal boundary layer, which increases the convective heat transfer coefficient and heat extraction from the receiver. However, feedwater flow velocity increased with $\dot{m}_f$, reducing residence time in the receiver, resulting in lower $T_{f,o}$.

4.4 Effect of receiver geometry

The ideal cavity receiver geometry uniformly distributes the incident heat flux, reducing peak flux absorption at any point on the surface. Heat losses in the receiver are significantly influenced by optical

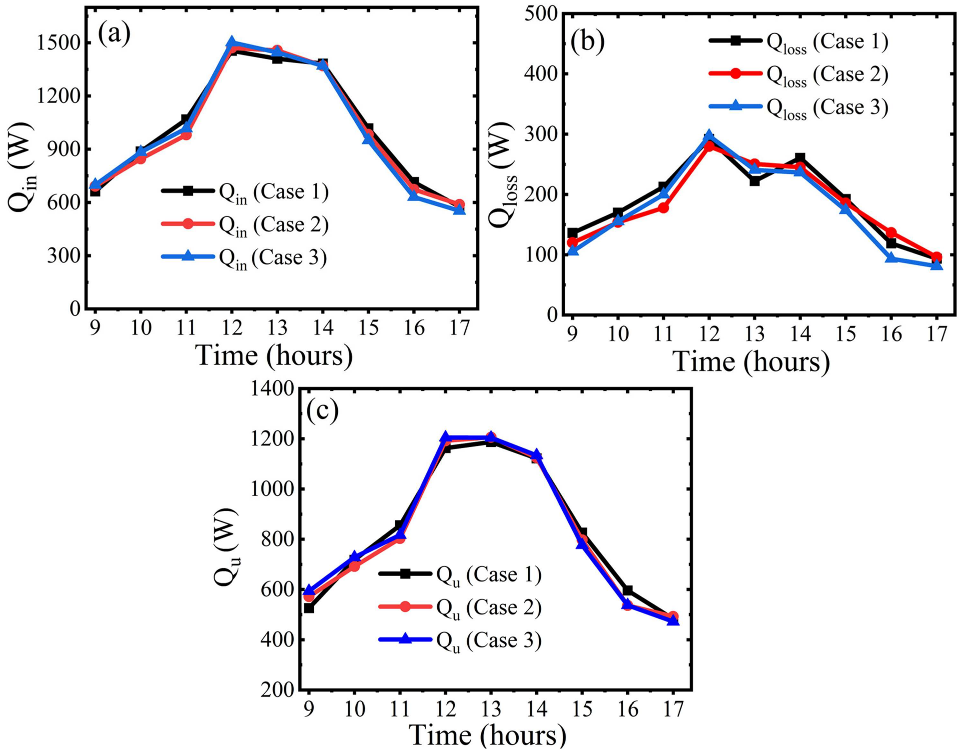

Figure 10. Effect of feedwater mass flow rate on (a) concentrated solar energy inside cavity ($\dot{Q}_{in}$), (b) cavity heat loss ($\dot{Q}_{loss}$), and (c) useful heat transfer to HTF ($\dot{Q}_u$) for the conical receiver under outdoor conditions.

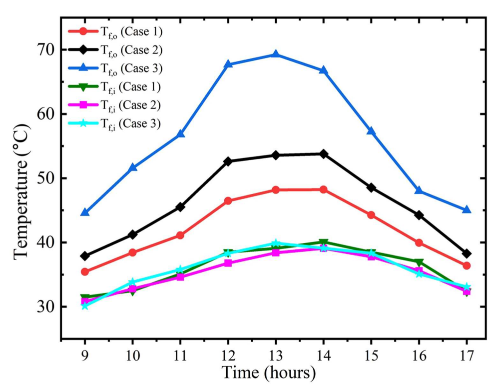

Figure 11. Effect of $\dot{m}_f$ on water outlet temperature ($T_{f,o}$).

Table 2. Feedwater outlet temperature for different $\dot{m}_f$.

Case	Case 1	Case 2	Case 3
Date	22/2/2025	24/2/2025	25/2/2025
$\dot{m}_f$ (kg/min)	0.5	1	1.5
Average G_T (W/m^2)	656	647	646
Average T_a (°C)	32.37	33.16	33.2
Average $T_{f,i}$ (°C)	36.07	35.36	35.91
Average $\dot{Q}_{in}$ (W)	1019	1006	1005
Average $\dot{Q}_{loss}$ (W)	186.5	183	177.5
Average $\dot{Q}_u$ (W)	830	824	829
Average $T_{f,o}$ (°C)	56.32	46.19	42.08

and geometrical properties. To optimize the geometry of the receiver, conical, spherical, and cylindrical shapes are tested. Figure 12 depicts the diurnal variation in G_T, T_a, and V_w during test days. In the experimental tests, the $\dot{m}_f$ was kept constant at 0.5 kg/min.

The test results are summarized in Table 3. Figure 13(a–c) shows the diurnal variation of heat transfer rates ($\dot{Q}_{\text{in}}$, $\dot{Q}_{\text{loss}}$, & $\dot{Q}_u$) for various receiver geometries (CR, SR, and CLR). Figure 13(b) indicates that the CR exhibited significantly lower $\dot{Q}_{\text{loss}}$ than the SR and CLR, by about 9.85% and 29.34%, respectively. Consequently, the $\dot{Q}_u$ in the CR is about 6.6–13.12% higher than in the SR and CLR. Figure 14 depicts the effect of receiver geometry on the overall heat loss coefficient (U_L). It can be noted from Table 3 that the highest U_L was observed for a CLR followed by SR and CR, resulting in higher $\dot{Q}_{\text{loss}}$ in the CLR. A CR has a lower U_L due to its reduced surface area to volume ratio, leading to lower $\dot{Q}_{\text{loss}}$ from exposed areas and higher heat absorption.

Figure 15(a and b) depicts the diurnal variation of the $T_{f,o}$ and heat removal factor, F_R, for various receiver geometries. The $T_{f,o}$ in all cavity receivers follow the G_T trend. As clearly seen in Figure 15(a), the CR consistently achieves a higher $T_{f,o}$ than the SR and CLR over a wide range of operating hours. As summarized in Table 3, the daily average $T_{f,o}$ of the CR is about 2.88–6.03% higher than that of the SR and CLR. This improvement is primarily attributed to the F_R of the conical receiver, as shown in Figure 15(b). It should be noted that the experiments were performed under outdoor conditions on different days using various receiver geometries to identify the optimal receiver configuration. Therefore, the performance comparison was not based solely on the $T_{f,o}$, but also on irradiance-normalized thermal performance parameters, including F_R, U_L, $\dot{Q}_u$, and U_L, which inherently account for variations in solar irradiance and operating conditions. These normalized parameters enable a fair and objective comparison of the receiver

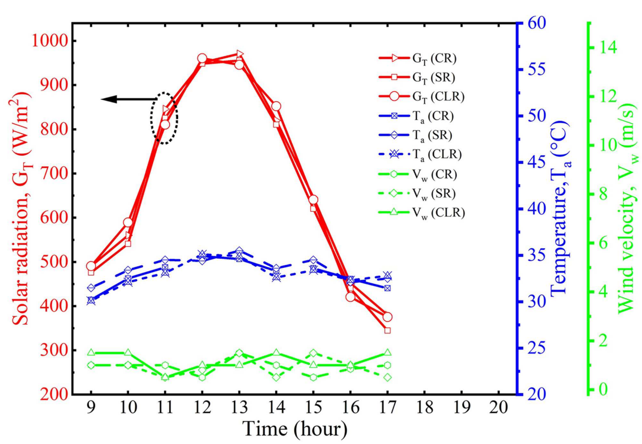

Figure 12. Diurnal variation of solar radiation (G_T), ambient temperature (T_a), and wind velocity (V_w) during outdoor experiments with different cavity receivers.

Table 3. Feedwater outlet temperature for different receiver geometry.

Receiver geometry	CR	SR	CLR
Date	1/3/2025	3/3/2025	5/3/2025
$\dot{m}_f$ (kg/min)	0.5	0.5	0.5
Average G_T (W/m^2)	679	676	662
Average T_a (°C)	32.91	33.55	32.93
Average $T_{f,i}$ (°C)	37.22	37.56	37.17
Average $\dot{Q}_{\text{in}}$ (W)	1057	1052	1031
Average $\dot{Q}_{\text{loss}}$ (W)	183	203	259
Average $\dot{Q}_u$ (W)	888	833	785
Average U_L (W/m^2 K)	34.91	42.86	50.87
Average F_R	0.66	0.64	0.62
Average $T_{f,o}$ (°C)	58.52	56.88	55.19

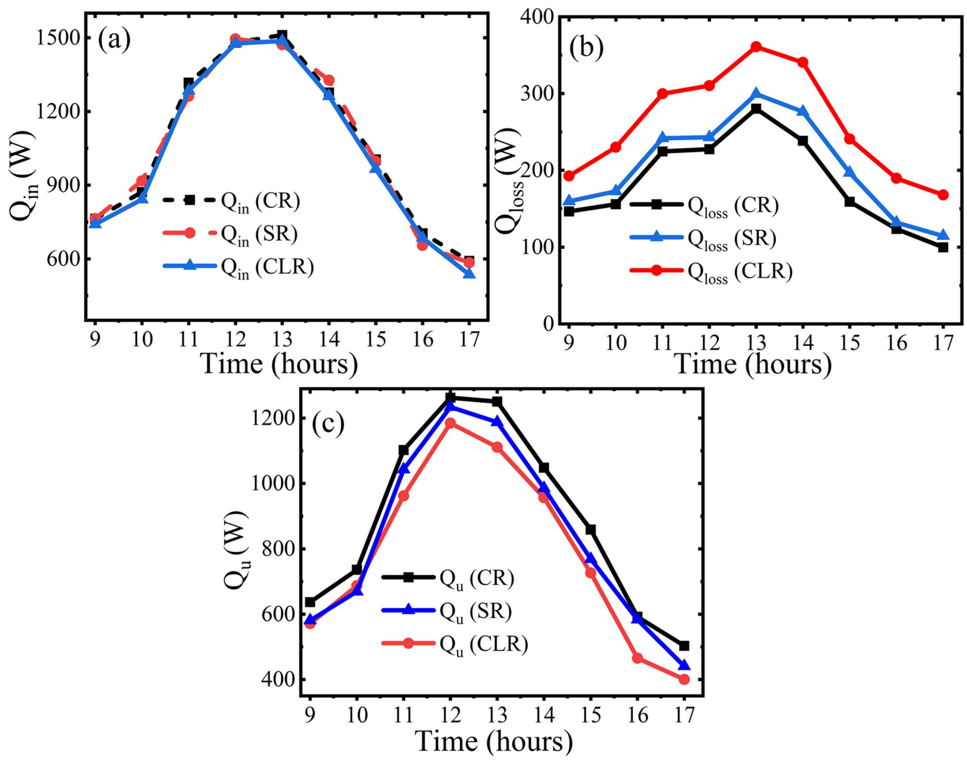

Figure 13. Effect of receiver geometry on (a) concentrated solar energy inside cavity ($\dot{Q}_{\text{in}}$), (b) cavity heat loss ($\dot{Q}_{\text{loss}}$), and (c) useful heat transfer to HTF ($\dot{Q}_u$).

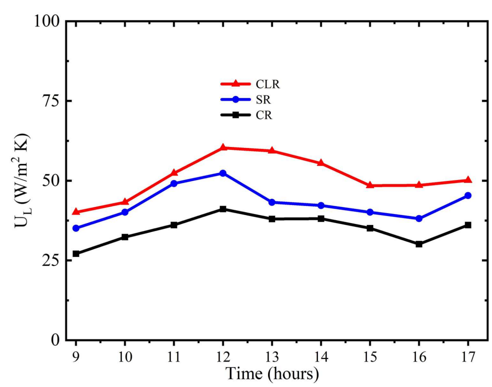

Figure 14. Effect of receiver geometry on overall heat loss coefficient (U_L).

geometries across different test days. Accordingly, based on the combined assessment of higher $T_{f,o}$, improved F_R, and lower U_L, as summarized in Table 3, the CR is identified as the optimal configuration for FLSCs.

4.5 Effect of CR length (L_{cr})

Increasing the L_{cr} improves the heat exchange area and thermal retention time, resulting in higher $T_{f,o}$. However, this leads to higher heat losses and uneven solar flux distribution. From an energy balance perspective (first law of thermodynamics), the $\dot{Q}_u$ in the cavity is primarily governed by the difference between the $\dot{Q}_{\text{in}}$ and $\dot{Q}_{\text{loss}}$. Hence, selecting the optimal L_{cr} is vital for improving thermal performance while minimizing losses. The FLSC was tested in outdoor conditions using CR of various lengths and

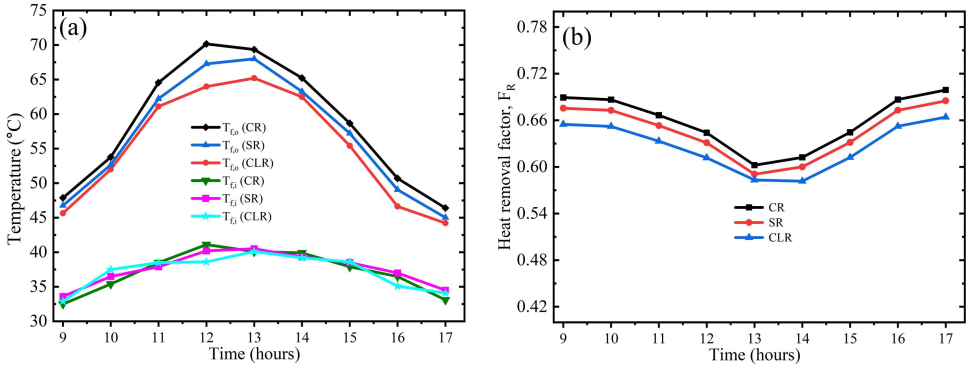

Figure 15. Effect of receiver geometry on (a) water outlet temperature ($T_{f,o}$) and (b) collector heat removal factor (F_R).

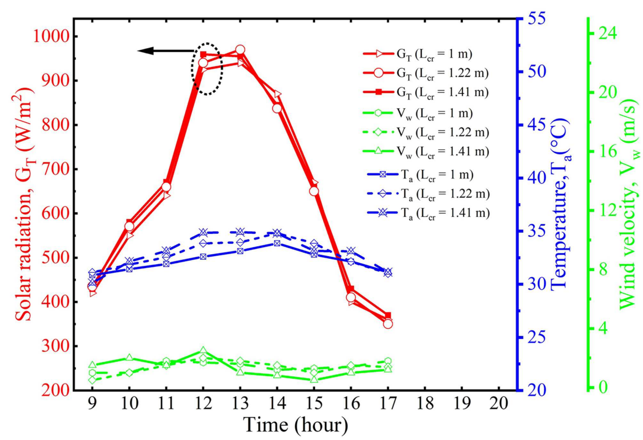

Figure 16. Diurnal variation of solar radiation (G_T), ambient temperature (T_a), and wind velocity (V_w) during outdoor experiments with different conical receiver lengths.

Table 4. Feedwater outlet temperature for different CR receiver lengths.

L_{cr} (m)	1	1.22	1.41
Date	8/3/2025	10/3/2025	11/3/2025
$\dot{m}_f$ (kg/min)	0.5	0.5	0.5
Average G_T (W/m^2)	642	648	655
Average T_a (°C)	32.19	32.79	33.01
Average $T_{f,i}$ (°C)	36.76	36.45	37.11
Average $\dot{Q}_{in}$ (W)	1003	1000	1007
Average $\dot{Q}_{loss}$ (W)	200	236	280
Average $\dot{Q}_u$ (W)	803	761	716
Average U_L (W/m^2 K)	37.61	45.6	53.12
Average F_R	0.65	0.63	0.60
Average $T_{f,o}$ (°C)	56.89	55.29	53.51

constant diameter. In the experimental tests, the $\dot{m}_f$ of 0.5 kg/min was maintained constant, and Figure 16 shows the diurnal variation of G_T. Table 4 summarizes the experimental findings. Figure 17(a–c) depicts the effect of L_{cr} on different heat transfer rates. It can be seen from Figure 17(b) that increasing the L_{cr} from 1 m to 1.41 m increased $\dot{Q}_{loss}$ by about 40%, resulting in a 10.83% decrease in $\dot{Q}_u$ in the cavity. This behavior can be explained using Newton's cooling law, where an increased heat exchange area enhances convective and radiative heat transfer to the surroundings. This, in turn, leads to an increase in the U_L. Figure 18 depicts the effect of L_{cr} on U_L. The L_{cr} increases the exposed area, leading to a higher U_L. Figure 19(a and b) illustrates the effect of L_{cr} on $T_{f,o}$ and F_R. It is worth noting that $T_{f,o}$ decreased with

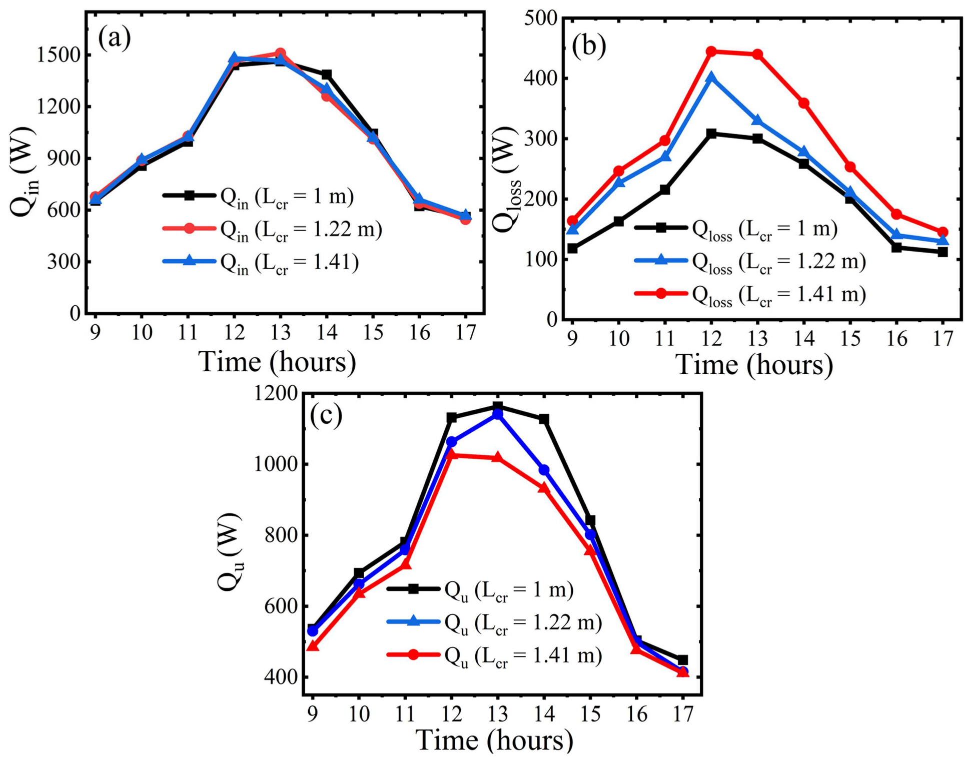

Figure 17. Effect of CR length on (a) concentrated solar energy inside cavity ($\dot{Q}_{\text{in}}$), (b) cavity heat loss ($\dot{Q}_{\text{loss}}$), and (c) useful heat transfer to HTF ($\dot{Q}_u$).

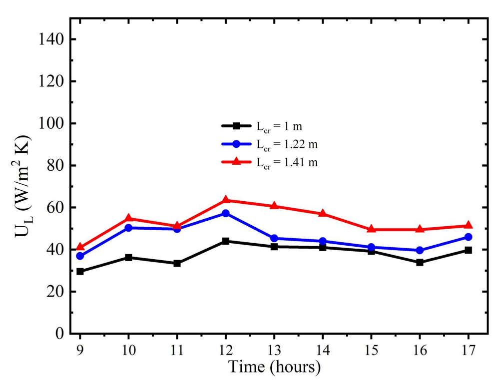

Figure 18. Effect of CR length on overall heat loss coefficient (U_L).

increasing L_{cr}. The day average $T_{f,o}$ obtained were 56.89 °C, 55.29 °C, and 53.51 °C, with L_{cr} of 1 m, 1.22 m, and 1.41 m, respectively. This is primarily due to the lower $\dot{Q}_u$ in the cavity (Figure 17(c))and the reduced F_R (Figure 19(b)). Therefore, 1 m was chosen as the optimal length for the CR.

4.6 Performance comparison

The performance comparison of the FLSC and the flat plate solar collector demonstrated that the FLSC achieved higher water outlet temperatures under similar conditions. In this study, the 2 m² FLSC with a CR achieved a maximum $T_{f,o}$ of 53–55 °C. This is significantly higher than the feedwater outlet temperatures reported for flat plate solar collectors, which were 47–48 °C (Sarwar et al. 2020) and 46–47 °C (Shaikh and Ismail 2023), respectively, at a $\dot{m}_f$ of 1 kg/min.

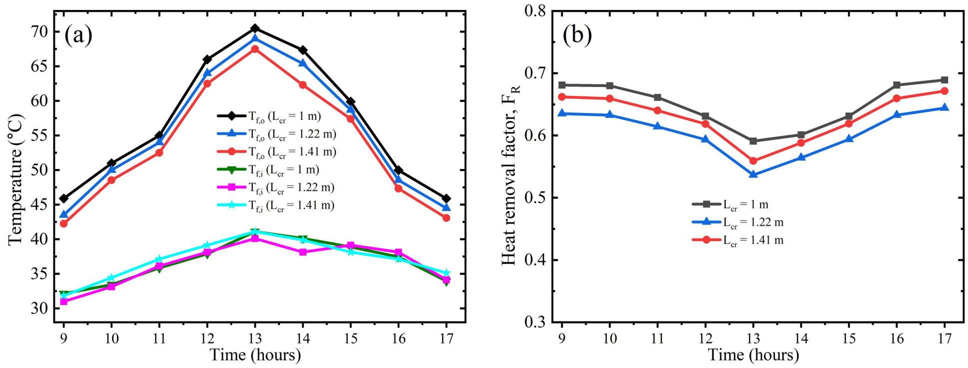

Figure 19. Effect of CR length on (a) water outlet temperature ($T_{f,o}$) and (b) collector heat removal factor (F_R).

4.7 Applicability and limitations

The present study demonstrates the potential applicability of the proposed FLSC with a conical receiver for several low- and medium-temperature applications, including:

- Solar water heating
- Solar desalination
- Industrial/process heating applications

The major limitations of the present work are summarized as follows:

- Only a limited number of cavity receiver geometries were investigated.
- Economic and techno-economic analyses were not included in the present study.
- Long-term experimental evaluation and seasonal performance analysis were not conducted.
- The developed thermo-optical model was based on certain simplifying assumptions.

5. Conclusions

In this study, a theoretical and experimental investigation of an FLSC with various receiver geometries, including conical, spherical, and cylindrical, has been carried out. The coupled thermal-optical model for the FLSC is developed and validated with outdoor experimental measurements. Based on the findings, the following conclusions are drawn:

- The receiver cavity temperature increased with solar intensity (G_T), resulting in higher heat losses. At a daily average G_T of 688 W/m²–707 W/m², the average feedwater outlet temperature ($T_{f,o}$) in the FLSC ranged from 52.51 °C–54.11 °C.
- The $\dot{m}_f$ exhibited a marginal effect on $\dot{Q}_{loss}$, $\dot{Q}_u$, and U_L. Although increasing the $\dot{m}_f$ from 0.5 kg/min to 1.5 kg/min reduced the thickness of the thermal boundary layer and increased the convective heat transfer coefficient, decreasing feedwater residence time in the receiver resulted in lower $T_{f,o}$.
- The conical receiver exhibited the lowest U_L, resulting in about 9.85–29.34% reduced $\dot{Q}_{loss}$ and 6.6–13.12% higher $\dot{Q}_u$ than spherical and cylindrical receivers. Furthermore, the maximum average $T_{f,o}$ and heat removal factor, F_R, of 58.52 °C and 0.66 were obtained with the conical receiver followed by the spherical receiver (56.88 °C and 0.64) and the cylindrical receiver (55.29 °C and 0.62).
- Increasing the length of the conical receiver from 1 m to 1.41 m reduced the day average $T_{f,o}$ from 56.89 °C to 53.51 °C due to increased exposed area, resulting in increased U_L and $\dot{Q}_{loss}$.

A performance comparison based on feedwater outlet temperature revealed that the FLSC with an optimal conical receiver geometry outperformed flat plate solar collectors. Future research may include optical flux distribution analysis using ANSYS ZEMAX coupled with thermal simulations to predict temperature distributions within cavity receivers, along with receiver coating optimization, evaluation of nanofluids, integration of thermal energy storage, and hybridization with other solar thermal technologies.

Author contributions

CRediT: **Vishwas Mahadeo Palve:** Conceptualization, Data curation, Formal analysis, Investigation, Methodology, Software, Validation, Writing – original draft; **Gajanan Namdeorao Shelke:** Conceptualization, Methodology, Project administration, Software, Supervision, Writing – review & editing.

Disclosure statement

No potential conflict of interest was reported by the author(s).

Funding

The author(s) reported there is no funding associated with the work featured in this article.

Notes on contributors

Vishwas Mahadeo Palve is the research scholar in the department of mechanical engineering at Department of Mechanical Engineering, Mumbai Educational Trust Institute of Engineering, Nashik, 422003, India. His research interests include renewable energy, solar collectors, and decentralized power production techniques.

Dr. Gajanan Namdeorao Shelke is the professor in the Department of Mechanical Engineering, Sandip Institute of Engineering and Management, Sandip Foundation, Nashik, 422213, India. His research interests are solar energy, desalination, distillation, IC engines, and renewable energy.

Data availability statement

No data was used for the research described in the article.

Nomenclature

Symbols

A	area (m^2)
a_m	accuracy of instrument
C_o	optical concentration ratio
C_p	specific heat (J/kg K)
D	diameter (m)
d	depth (m)
D_{turn}	receiver coils turn diameter (m)
F_R	collector heat removal factor
G_T	global solar radiation (W/m^2)
Gr_a	Grashof number
h	heat transfer coefficient (W/m^2 K)
k	thermal conductivity (W/m K)
L	length (m)
$\dot{m}$	mass flow rate (kg/s)
Nu	Nusselt number
Pr	Prandtl number
$\dot{Q}$	heat transfer rate (W)
Re	Reynolds number
S	energy absorbed per unit receiver surface area (W/m^2)
T	temperature (°C)
t	thickness (m)
U_L	overall heat loss coefficient (W/m^2 K)
u_m	uncertainty of instrument

V_w wind speed (m/s)
W width (m)

Greek letters

ε emissivity
δ_R uncertainty in calculated parameter
σ Stefan–Boltzmann constant (W/m^4 K)
μ dynamic viscosity (Pa-s)
η_{opt} optical efficiency
α_f absorptive factor
α_c absorptivity of cavity wall
θ vertex angle (°)
θ_{cv} cavity tilt angle (°)

Subscripts

a ambient air
cr conical receiver
cv cavity
clr cylindrical receiver
cond conduction
conv convection
eff effective
f fluid
for force
i inside
in inlet
ins insulation
m mean
nat natural
o outside/outlet
r receiver coil
rad radiation
sc solar collector
sr spherical receiver
u useful

Acronyms

CL conical receiver
CLR cylindrical receiver
CST concentrating solar technology
FL Fresnel lens
FLSC Fresnel lens solar collector
HLC heat loss coefficient
HTF heat transfer fluid
SR spherical receiver

References

Aboelmaaref, M. M., J. Zhao, W. Li, E. S. Ali, A. A. Askalany, M. Ghazy, L. Gu, and M. E. Zayed. 2023. "Research on Solar dish/Stirling Engine Driven Adsorption-Based Desalination System for Simultaneous Co-Generation of Electricity and Freshwater: Numerical Investigation." *Case Stud. Therm. Eng.* 47: 103044. https://doi.org/10.1016/j.csite.2023.103044.

Al-Dafaie, A. M. A., M. E. Dahdolan, and M. A. Al-Nimr. 2016. "Utilizing the Heat Rejected from a Solar Dish Stirling Engine in Potable Water Production." Solar Energy 136: 317–326. https://doi.org/10.1016/j.solener.2016.07.007.

Banakar, A., A. Motevali, M. Emad, and B. Ghobadian. 2017. "Co-Generation of Heat and Power in a Thermoelectric System Equipped with Fresnel Lens Collectors Using Active and Passive Cooling Techniques." *Renew. Energy* 112: 268–279. https://doi.org/10.1016/j.renene.2017.05.052.

Cengel, Y. A. and A. J. Ghajar. 2007. Heat & Mass Transfer: A Practical Approach. In *Pvt Limited*. 2007. 4th ed. India: McGraw-Hill Education.

Daabo, A. M., S. Mahmoud, and R. K. Al-Dadah. 2016. “The Optical Efficiency of Three Different Geometries of a Small Scale Cavity Receiver for Concentrated Solar Applications.” Applied Energy 179: 1081–1096. https://doi.org/10.1016/j.apenergy.2016.07.064.

Duffie, J. A. and W. A. Beckman. 2002. *Solar Engineering of Thermal Processes*. fourth ed., John Wiley & Sons.

Garg, K., S. K. Das, and H. Tyagi. 2022. “Thermal Design of a Humidification-Dehumidification Desalination Cycle Consisting of Packed-Bed Humidifier and Finned-Tube Dehumidifier.” *Int. J. Heat Mass Transf.* 183: 122153. https://doi.org/10.1016/j.ijheatmasstransfer.2021.122153.

González-Camarillo, H., A. Gallo, I. Padilla, C. A. Pérez-Rábago, C. A. Asselineau, M. Romero, and A. López-Delgado. 2024. “Design Solutions and Characterization of a Small Scale and Very High Concentration Solar Furnace Using a Fresnel Lens.” Applied Thermal Engineering 255: 124044. https://doi.org/10.1016/j.applthermaleng.2024.124044.

Jensen, A. R., I. Sifnaios, G. P. Caringal, S. Furbo, and J. Dragsted. 2022. “Thermal Performance Assessment of the World's First Solar Thermal Fresnel Lens Collector Field.” Solar Energy 237: 447–455. https://doi.org/10.1016/j.solener.2022.01.067.

Jilte, R. D., S. B. Kedare, and J. K. Nayak. 2014. “Investigation on Convective Heat Losses from Solar Cavities under Wind Conditions.” Energy Procedia 57: 437–446. https://doi.org/10.1016/j.egypro.2014.10.197.

Kabeel, A. E., and M. Abdelgaied. 2018. “Experimental Evaluation of a Two-Stage Indirect Solar Dryer with Reheating Coupled with HDH Desalination System for Remote Areas.” Desalination 425: 22–29. https://doi.org/10.1016/j.desal.2017.10.016.

Lawal, D. U., M. A. Antar, A. Khalifa, S. M. Zubair, and F. Al-Sulaiman. 2020. “Experımental Investigation of Heat Pump Driven Humidification-Dehumidification Desalination System for Water Desalination and Space Conditioning.” Desalination 475: 114199. https://doi.org/10.1016/j.desal.2019.114199.

Le Quere, P., F. Penot, and M. Mirenayat. 1981. Experimental Study of Heat Loss through Natural Convection from an Isothermal Cubic Open Cavity In *Proceedings DOE/SERI/SNLL Workshop on Convective Losses from Solar Receivers*. P. K. Falcone, ed. 165e174. Livermore, California, Sandia Laboratory Report SAND81-8014.

Le Roux, W. G., T. Bello-Ochende, and J. P. Meyer. 2014. “The Efficiency of an Open-Cavity Tubular Solar Receiver for a Small-Scale Solar Thermal Brayton Cycle.” *Energy Convers. Manag.* 84: 457–470. https://doi.org/10.1016/j.enconman.2014.04.048.

Lin, M., K. Sumathy, Y. J. Dai, and X. K. Zhao. 2014. “Performance Investigation on a Linear Fresnel Lens Solar Collector Using Cavity Receiver.” Solar Energy 107: 50–62. https://doi.org/10.1016/j.solener.2014.05.026.

Loni, R., A. B. Kasaeian, E. Askari Asli-Ardeh, and B. Ghobadian. 2016. “Optimizing the Efficiency of a Solar Receiver with Tubular Cylindrical Cavity for a Solar-Powered Organic Rankine Cycle.” Energy 112: 1259–1272. https://doi.org/10.1016/j.energy.2016.06.109.

Mendoza Castellanos, L. S., G. E. Carrillo Caballero, V. R. Melian Cobas, E. E. Silva Lora, and A. M. Martinez Reyes. 2017. “Mathematical Modeling of the Geometrical Sizing and Thermal Performance of a Dish/Stirling System for Power Generation.” *Renew. Energy* 107: 23–35. https://doi.org/10.1016/j.renene.2017.01.020.

Mokhtar, G., B. Boussad, and S. Noureddine. 2016. “A Linear Fresnel Reflector as a Solar System for Heating Water: Theoretical and Experimental Study.” *Case Stud. Therm. Eng.* 8: 176–186. https://doi.org/10.1016/j.csite.2016.06.006.

Penot, F. 1982. “Numerical Calculation of Two-Dimensional Natural Convection in Isothermal Open Cavities.” *Numerical Heat Transfer* 5: 421e437. https://doi.org/10.1080/10407788208913457.

Perini, S., X. Tonnellier, P. King, and C. Sansom. 2017. “Theoretical and Experimental Analysis of an Innovative Dual-Axis Tracking Linear Fresnel Lenses Concentrated Solar Thermal Collector.” Solar Energy 153: 679–690. https://doi.org/10.1016/j.solener.2017.06.010.

Prakash, M., S. B. Kedare, and J. K. Nayak. 2012. “Numerical Study of Natural Convection Loss from Open Cavities.” International Journal of Thermal Sciences 51: 23–30. https://doi.org/10.1016/j.ijthermalsci.2011.08.012.

Qiu, K., L. Yan, M. Ni, C. Wang, G. Xiao, Z. Luo, and K. Cen. 2015. “Simulation and Experimental Study of an Air Tube-Cavity Solar Receiver.” *Energy Convers. Manag.* 103: 847–858. https://doi.org/10.1016/j.enconman.2015.07.013.

Reddy, K. S., T. S. Vikram, and G. Veershetty. 2015. “Combined Heat Loss Analysis of Solar Parabolic Dish - Modified Cavity Receiver for Superheated Steam Generation.” Solar Energy 121: 78–93. https://doi.org/10.1016/j.solener.2015.04.028.

Ruelas, J., N. Velázquez, and J. Cerezo. 2013. “A Mathematical Model to Develop a Scheffler-Type Solar Concentrator Coupled with a Stirling Engine.” Applied Energy 101: 253–260. https://doi.org/10.1016/j.apenergy.2012.05.040.

Sarwar, J., M. R. Khan, M. Rehan, M. Asim, and A. H. Kazim. 2020. “Performance Analysis of a Fl at Plate Collector to Achieve a Fi Xed Outlet Temperature under Semi-Arid Climatic Conditions.” Solar Energy 207: 503–516. https://doi.org/10.1016/j.solener.2020.06.088.

Shaikh, J. S., and S. Ismail. 2023. “The Potential of Sweeping Gas Membrane Distillation Integrated with Multistage Bubble Column Dehumidifier in Recovering Potable Water from Wastewater Contaminated with Industrial Metalworking Fluid.” *Chem. Eng. Process. - Process Intensif.* 194: 109584. https://doi.org/10.1016/j.cep.2023.109584.

Shaikh, J. S., and S. Ismail. 2023. “Theoretical Investigation on humidification–dehumidification Desalination Employing Flat-Plate Solar Water Collector.” Journal of Thermal Analysis and Calorimetry 148: 11835–11853. https://doi.org/10.1007/s10973-023-12478-6.

Sharma, S., S. K. Saha, S. B. Kedare, and S. Singh. 2020. “Experimental and Numerical Study of Thermal Performance of Helical Coil Receiver with Fresnel Lens.” Applied Thermal Engineering 165: 114608. https://doi.org/10.1016/j.applthermaleng.2019.114608.

Shen, Z. G., S. Y. Wu, L. Xiao, and Z. X. Chen. 2017. "Proposal and Assessment of a Solar Thermoelectric Generation System Characterized By Fresnel Lens, Cavity Receiver and Heat Pipe." Energy 141: 215–238. https://doi.org/10.1016/j.energy.2017.09.051.

Wang, H., J. Huang, M. Song, and J. Yan. 2019. "Effects of Receiver Parameters on the Optical Performance of a Fixed-Focus Fresnel Lens Solar Concentrator/Cavity Receiver System in Solar Cooker." Applied Energy 237: 70–82. https://doi.org/10.1016/j.apenergy.2018.12.092.

Xie, W. T., Y. J. Dai, and R. Z. Wang. 2011. "Numerical and Experimental Analysis of a Point Focus Solar Collector Using High Concentration Imaging PMMA Fresnel Lens." *Energy Convers. Manag.* 52: 2417–2426. https://doi.org/10.1016/j.enconman.2010.12.048.

Xie, W. T., Y. J. Dai, and R. Z. Wang. 2013. "Thermal Performance Analysis of a Line-Focus Fresnel Lens Solar Collector Using Different Cavity Receivers." Solar Energy 91: 242–255. https://doi.org/10.1016/j.solener.2013.01.029.

Xie, W. T., Y. J. Dai, and R. Z. Wang. n.d. Numerical and Experimental Analysis of a Point Focus Solar Collector Using High Concentration Imaging PMMA Fresnel Lens. Elsevier Ltd. https://doi.org/10.1016/j.enconman.2010.12.048

Zayed, M. E., J. Zhao, A. H. Elsheikh, Z. Zhao, S. Zhong, and A. E. Kabeel. 2021. "Comprehensive Parametric Analysis, Design and Performance Assessment of a Solar dish/Stirling System." Process Safety and Environmental Protection 146: 276–291. https://doi.org/10.1016/j.psep.2020.09.007.

Zhai, H., Y. J. Dai, J. Y. Wu, R. Z. Wang, and L. Y. Zhang. 2010. "Experimental Investigation and Analysis on a Concentrating Solar Collector Using Linear Fresnel Lens." *Energy Convers. Manag.* 51: 48–55. https://doi.org/10.1016/j.enconman.2009.08.018.